Assessment of Satellite Imagery Capability for Damage Detection Using Landsat 7/ETM+ Images for the 2001 Atico, Peru Earthquake

By

Miguel ESTRADA[1], Masayuki KOHIYAMA[2] and Fumio YAMAZAKI[3]

ABSTRACT

For the evaluation of damage after a natural disaster occurs different methods exist. As a result of the progress and advances in remote sensing technologies as well as information that may be readily obtained from civilian satellites, satellite imagery is gaining acceptation nowadays for damage detection. In this paper the capability of remotely sensed images to evaluate the damage caused by the 2001 Atico, Peru earthquake is assessed. The utilized images were taken by the Landsat 7 satellite, which carries on board the Enhanced Thematic Mapper Plus sensor. The method for the assessment is the evaluation of the results of different approaches for damage detection. The damage detection techniques are based on the comparison of two sets of images taken at different times, in this case the two sets are those taken before and after the earthquake. Three different methods have been applied for damage detection: rationing of bands in the visible range, image correlation analysis and principal component analysis. Among them the method of image correlation showed a clear tendency in the pixel values, with low values for sectors of high damage and high values of correlation for sectors of less damage.

Key words: The 2001 Atico-Peru earthquake, damage detection, Landsat 7/ETM+, image correlation, image enhancement.

Introduction

After a natural disaster occurs it is important to know the distribution and extent of the damage. Due to the collapse or heavy damage of infrastructure facilities, like lines of communication and roads, the damage information in remote places may take long time to reach the decision-makers and therefore the emergency response and recovery plans could be delayed. Several methods exist for the recognition of affected areas: field survey reconnaissance, the use of aerial photographs, and recently the use of videos taken from airplanes as well as the use of satellite imagery (Matsuoka and Yamazaki, 2000). Kohiyama *et al.* (2000) have reported the estimation of damage areas due to the 1999 Chi-Chi, Taiwan earthquake by estimating the significant reductions or loss of lights in nighttime by using images taken by the Defense Meteorological Satellite Program (DMSP). Landsat 5/TM images were utilized to evaluate the damage in the cities of Gölcük and Adapazari, due to the 1999 Kocaeli, Turkey earthquake (Estrada *et al.*, 2001).

In this paper the use of remotely sensed images taken by Landsat 7/ETM+ to determine the damage due to the 2001 Atico, Peru earthquake has been attempted. The assessment of the use of satellite imagery is carried out by comparing the results of three methods for damage detection. For the first method, the ratio of the normalized difference indices of the post- and pre-event image are calculated. The second method is the image correlation analysis and finally the last method is the use of the principal component transformation.

The study area is the city of Moquegua located in southern Peru (1,144 km from Lima, the capital city, see Figure 1). Moquegua was one of the most heavily affected cities due to the earthquake, along with the cities of Arequipa, Tacna and Camana among others. As a consequence of the earthquake the department of Moquegua had a toll of 25 deaths, 341 injured, 53,448 affected people, 5,505 collapsed houses and 5,469 damaged houses (INDECI, 2001). The damage in Moquegua City was proportionally larger due to the concentration of adobe houses.

[1] Graduate Student, Institute of Industrial Science, The University of Tokyo, Japan.
[2] Research Associate, ditto.
[3] Professor, Asian Institute of Technology, Thailand.

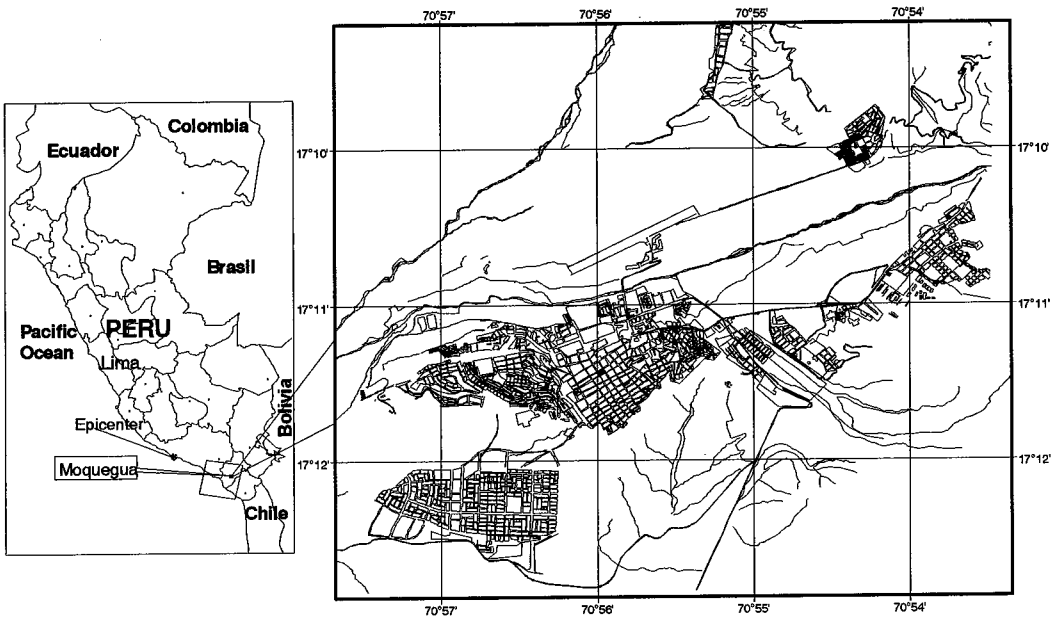

Figure 1. Map of the study area. The main map shows the areas of the Moquegua City.

Generally, change detection techniques for remotely sensed images are based on applying specialized algorithm to two satellite images of the same area acquired at different times. The algorithm examines every pixel in the two scenes to determine which pixel values have changed. The images taken by the Landsat 7/ETM+ have a spatial resolution or ground instant field of view (GIFOV) of 30 meters for the visible and near infrared bands that does not allow to recognize houses or object smaller than the GIFOV. However, it is possible to detect objects that are considerably smaller than the GIFOV if their contrast to the surrounding background is sufficiently high (Schowengerdt, 1997). Thus, if the collapse of houses due to an earthquake causes the spread of debris, this dispersal may affect the reflectance of the adjacent areas. Then changes in the pixels values may occur and may be detected.

Landsat 7/ETM+ images taken at different dates have been used to study the effects of the 2001 Atico, Peru earthquake. The pre-event set was acquired on May 26, 2001, 28 days before the earthquake, while the post-event set was taken on June 27, 2001, 4 days after the event (Figure 2). Table 1 summarizes the characteristics of these images. A digital map of Moquegua City at scale 1:25,000 is also available (Figure 1).

Table 1. Characteristics of the used satellite images.

Acquisition Date (the pre- and post-event)	2001/05/26 and 2001/06/27
Satellite/Sensor	Landsat 7/Enhanced thematic mapper plus
Visible Bands (spectral range in μm)	B1 (0.45 - 0.515), B2 (0.525 - 0.605), B3 (0.63 - 0.690)
Near Infrared bands (spectral range in μm)	B4 (0.75 - .90), B5 (1.55 - 1.75), B7 (2.09 - 2.35)
Thermal infrared band (spectral range in μm)	B6 (10.40 - 12.50)
Panchromatic band (spectral range in μm)	Pan (0.52 - 0.90)
Sun angles (pre, post)	Elevation (40.8°, 39.8°), Azimuth (38.3 39.5)
Correction Level	Systematic (Level 1G)
Rows/Columns	6888/7389
Ground resolution (meters)	VNIR(30), TIR(60), PAN(15)*

* VNIR stands for Visible and near infrared bands, TIR stands for thermal infrared band and PAN stands for panchromatic band.

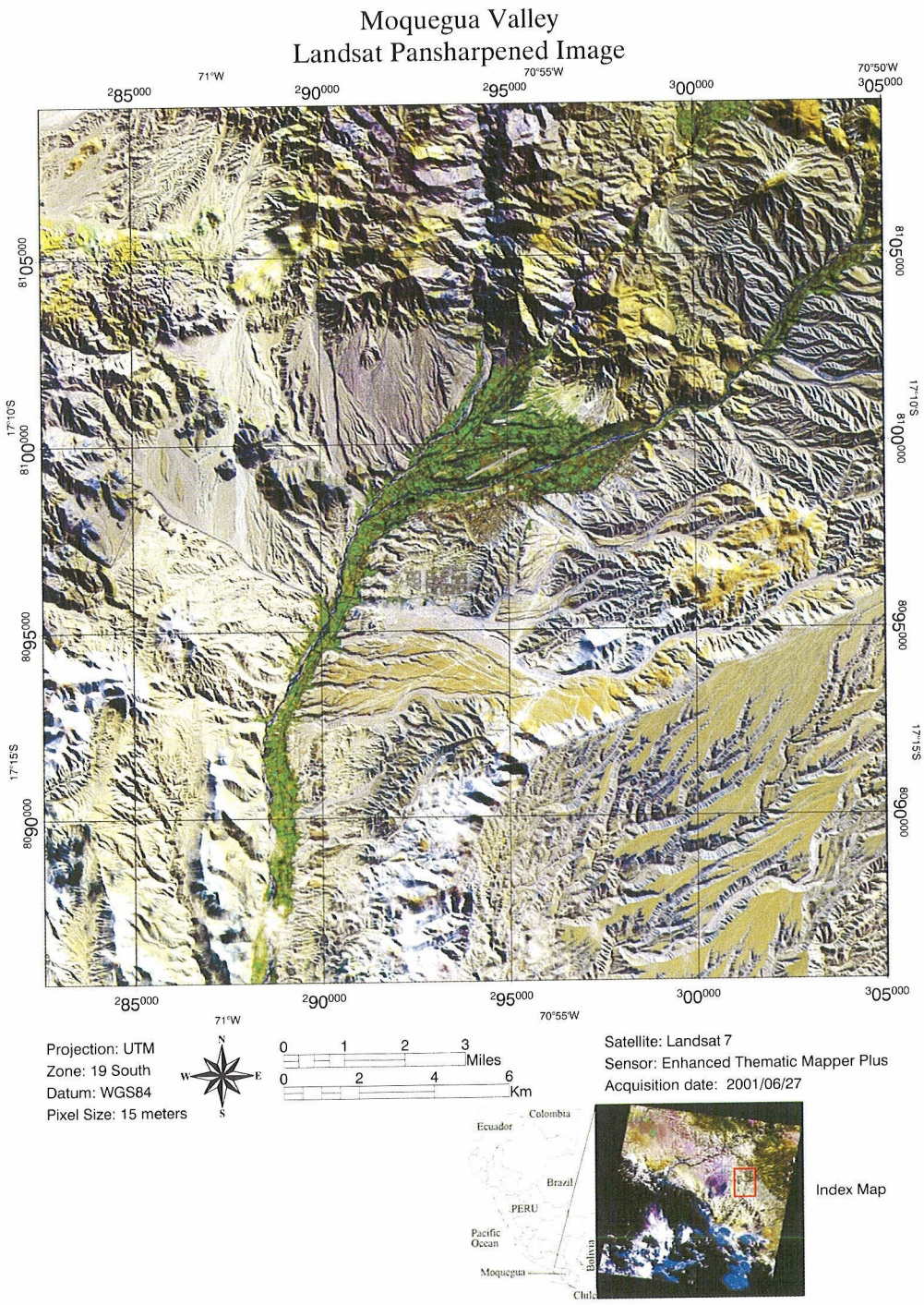

Figure 2: Pansharpened Landsat image of Moquegua Valley. Moquegua City is located in the center of the image. The index map shows the whole satellite image. This enhanced image has been obtained by merging bands 1, 2 and 3, (30 meters ground resolution) with the panchromatic one (15 meters resolution).

Pre-processing of satellite imagery

Atmospheric Correction

The atmosphere affects the radiance measured at any point in the scene in two ways: firstly, it attenuates the energy illuminating a ground object and secondly it acts as a reflector itself, redirecting some of the incoming electromagnetic energy within the atmosphere into the field of view of the sensor; this is called the atmospheric path radiance. Thus the composite signal observed at any given location can be expressed (Lillesand, 2000) by:

$$L_{tot} = \frac{\rho ET}{\pi} + L_p \quad (1)$$

Where:

L_{tot} = total spectral radiance measured by sensor
ρ = reflectance of object
E = irradiance on object
T = transmission of atmosphere
L_p = path radiance

L_p represents the scattered path radiance that introduces haze in the imagery and reduces image contrast. In case of Landsat images band 1 will generally have a high value of L_p component, higher than bands 2 and 3. For the mid-infrared bands the path radiance has minor effects.

The regression method (Mather, 1999) is a simple method to estimate the path radiance and has the advantage of using information present within the image itself. This method is applicable to areas of image that have known brightness; as could be dark features (clear water or deep shadows), these pixels will have values very close to zero in the near-infrared band (Band 4 in case of Landsat 7/ETM+). By using the scatter diagrams for multispectral data, the pixels values of band 4 of dark features are plotted against the pixel values of the bands 1, 2 and 3. Then best-fit straight lines are computed using standard regression methods (least squares). An approximation of the path radiance is given by the intercept of the regression line with the X-axis. Finally, this value is subtracted from the respective image. Figure 3 shows the scatter plots of the pre- and post-event bands and the results are summarized in Table 2.

Table 2. Path radiance correction (PRC) and correlation coefficient (r) for the pre- and post-event visible bands.

Band	Pre-event		Post-Event	
	PRC	r	PRC	r
Band 1	22.94	0.906	21.75	0.902
Band 2	8.98	0.935	9.45	0.940
Band 3	2.71	0.960	2.73	0.957

Geographic Correction

In order to make the comparison between the pre- and post-event images, very accurate registration of images is required. To have the satellite image geographically registered, GIS based maps are used. The geographic correction of the images was carried out through the image-to-map registration in which ground control points are interactively selected both in the image and in the digital map. These control points should be well deployed over the map to avoid distortions when the warping process is carried out. The number of identified ground control points was 25 yielding a RMS error of 0.32 pixels. Finally, for the registration of the images a second order polynomial equation for the transformation and rotation of the image and the nearest neighborhood resampling technique for interpolation, were used. Figure 4 shows the location of the ground control points.

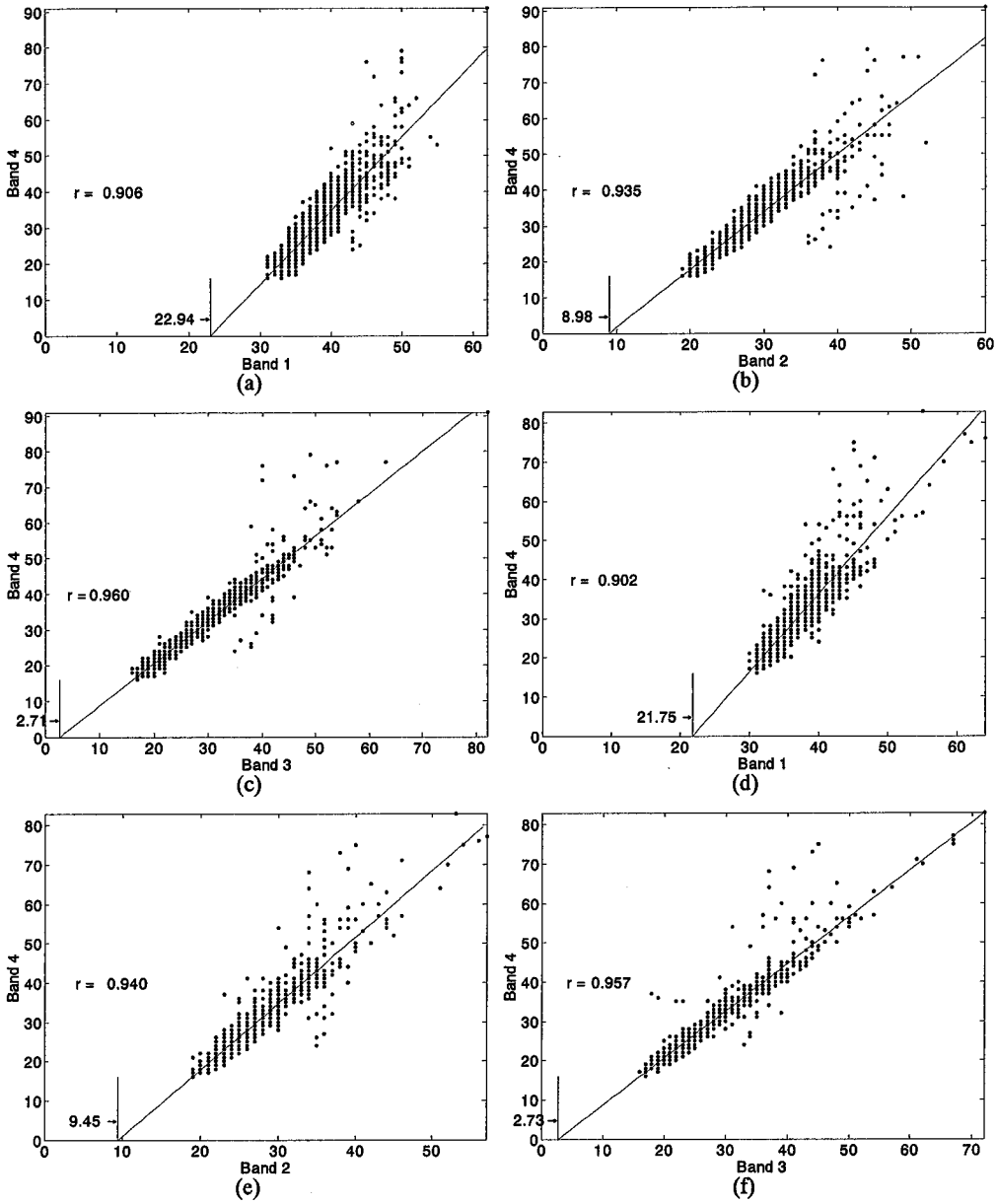

Figure 3. Regression method for the estimation of the atmospheric path radiance. (a), (b) and (c) show the scatter plots of Band 4 vs. Bands 1, 2 and 3 of the pre-event image respectively. (d), (e) and (f) are the same for the post-event image.

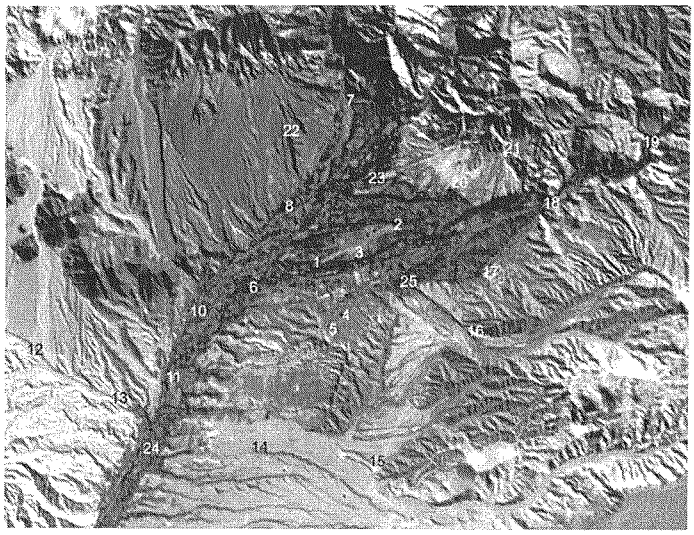

Figure 4. Deployment of ground control points for the image-to-map geographic correction.

Integration of remote sensing imagery with GIS data

In order to identify the different sectors in Moquegua City, a digital map was integrated with the remote sensing images. The digital map, initially in CAD format at block level, was converted to a GIS based format and then the blocks were grouped into sectors to conduct an analysis, to overcome the limitation of ground resolution. According to the information from the Japan-Peru Center for Earthquake Engineering and Disaster Mitigation (CISMID) the sectors with higher levels of damage were Cercado (the downtown) and San Francisco, followed by Mariscal Nieto, El Siglo and San Antonio. To develop a method of damage detection, ancillary information is necessary to calibrate any model or any proposed method. Once a methodology is completely developed, it is hoped that the recognition of different levels and extent of damage can be automatically done. Figure 5 shows the integration of the GIS map with the remotely sensed image.

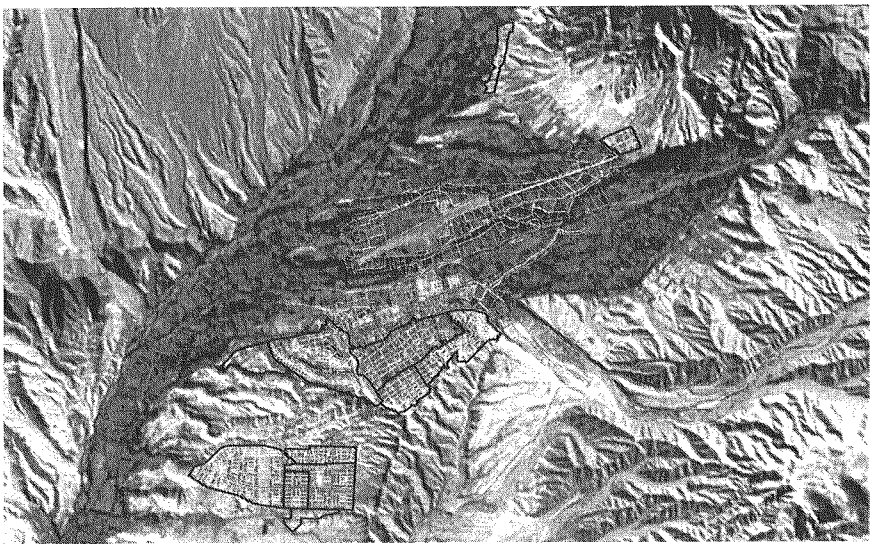

Figure 5. In order to identify the different sectors of Moquegua City, GIS information is incorporated with the remote sensing imagery.

Image enhancement

Colors are formed by the combination of different amounts of red, green and blue lights. Figure 6(a) shows a geometrical representation of the RGB model color cube. The origin of this cube is black and the coordinates are given for values over the axes red, green and blue. Notice that white light is formed by the addition of maximum red, green and blue. The HSI model uses the concepts of hue (H), saturation (S) and intensity (I) to explain the idea of color. Hue refers to the dominant or average wavelength of light contributing to a color. Saturation specifies the purity of color relative to gray. Intensity relates to the total brightness of color. Figure 6(b) shows a 3D geometrical representation (hexcone) of the HSI model. Hue is represented by angular position around the top of the hexcone (e.g. red at 0°, green at 120°, and blue at 240°). The saturation is determined by the distance from the center, vertical axis of the hexcone to any point in the hexagon. Intensity is defined by the distance along the gray line, from black to any given hexagonal projection. Any pixel in the RGB color space can be transformed into its HSI counterpart and vice versa.

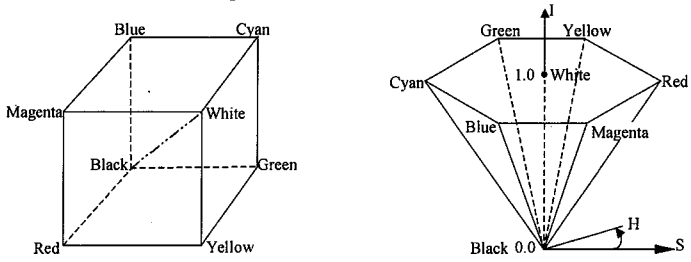

(a) (b)

Figure 6. The color space. (a) Red-green-blue color cube. (b) Hue-saturation-intensity hexcone.

The HSI transform is used as a means of combining co-registered images of different resolution or sources. First RGB bands (i.e. Bands 3, 2 and 1) are converted into HSI and the spatial resolution is changed to match the image with high resolution, and then the intensity component is replaced by the high resolution data (band 8 in case of Landsat 7). Finally, this new H', S', I' image is converted back to R', G', B'. Figure 7 shows the results of this enhancement over Moquegua City. The process of transformation is described as follows:

a) RGB to HSI transformation:
First the RGB values have to be normalized by their maximum values so that the ranges of R, G, and B are [0, 1]. The ranges of S and I are also [0, 1] and the range of H is [0, 2π]. Intensity I is given:
I=max(R, G, B)
Saturation S and hue H are given as follows:
If I=0; then S=0 and H=indeterminate.

If $I\neq0$, then $S=(I-i)/I$, where i=min(R, G, B),
and if $R=I$ then $H=(g-b)\pi/3$
if $G=I$ then $H=(2+r-b)\pi/3$
if $B=I$ then $H=(4+g-r)\pi/3$, where $r=(I-R)/(I-i)$, $g=(I-G)/(I-i)$, $b=(I-B)/(I-i)$.

b) HSI to RGB transformation:
Once the image has been manipulated, it must be transformed back into the RGB so that the image can be displayed. The transformation from HSI to RGB is as follows:

If S=0, $R=G=B=I$ regardless of value of H.
If $S\neq0$, then: If h=0 then: $R=I$, $G=T$, and $B=P$
If h=1 then: $R=Q$, $G=I$, and $B=P$

If h=2 then: R=P, G=I, and B=T
If h=3 then: R=P, G=Q, and B=I
If h=4 then: R=T, G=P, and B=I
If h=5 then: R=I, G=P, and B=Q

where: $H'=3H/\pi$, h=floor(H'), $P=I(1-S)$,
$Q=I\{1-S(H'-h)\}$, and $T=I\{1-S(1-H'+h)\}$
(floor(x): function of getting the truncated value of x).

Figure 7 shows an example of this image enhancement.

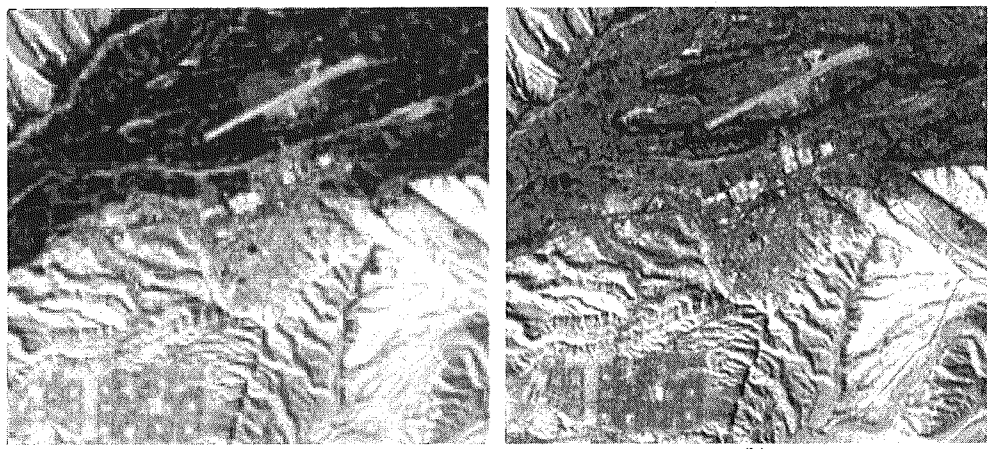

(a) (b)

Figure 7. Image enhancement done by HSI transformation. (a) Raw image 30 meters resolution. (b) Pansharpened (enhanced) image with 15 meters resolution.

Image Analysis

Normalized ratios

One of the simplest techniques of feature extraction applied to remote sensing images is the calculation of the ratio of digital number of different bands. Additionally to simple band rationing the Normalized Difference Vegetation Index (NDVI) is broadly used to indicate vegetation conditions. Based on the basic idea of the NDVI other normalized indices can be obtained by combining the different bands in the visible range of the spectrum. In this paper three kinds of normalized indices have been used based on the first three bands of the image set, they are:

$$\begin{aligned} R1 &= (B1 - B2)/(B1 + B2), \\ R2 &= (B1 - B3)/(B1 + B3), \text{ and} \\ R3 &= (B2 - B3)/(B2 + B3). \end{aligned} \tag{2}$$

Once these three normalized ratios have been obtained for the pre-event and post-event images, the following second ratios are computed to see if changes can be detected. The second ratios are evaluated as follows:

$$\begin{aligned} SR1 &= R1_{after} / R1_{before}, \\ SR2 &= R2_{after} / R2_{before}, \text{ and} \\ SR3 &= R3_{after} / R3_{before}. \end{aligned} \tag{3}$$

The mean values and standard deviations of these ratios in the five sectors in Moquegua City are shown in Figure 8. The sectors are ordered by its level of damage, from higher to minor damage.

Figures 8(a) and (b) do not show a clear pattern on the behavior of the ratio, however, Figure8(c) shows that for higher level of damage the ratio SR3 is greater than 1 and descends along with the lower level of damage. Although a tendency can be observed in the values of the ratio SR3, it should be noticed that the standard deviations are considerably large.

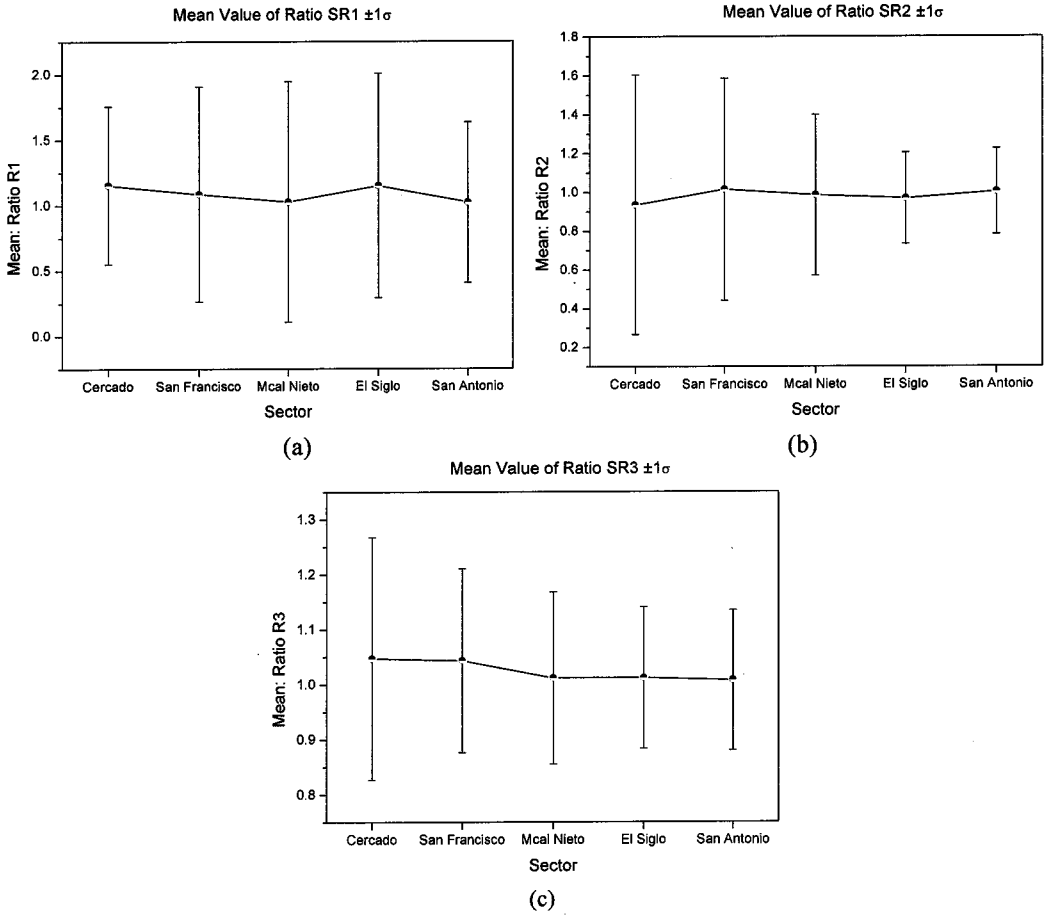

Figure 8. Mean values and standard deviations of ratios SR1, SR2 and SR3. Notice that there is a decreasing trend in ratio SR3 along with the level of damage, from heavy to slight damage.

Image Correlation Analysis

Correlation analysis is the statistical tool that can be used to describe the degree to which two variables are "correlated" to each other. It is very common to use a correlation analysis for automated detection of ground control points for image-to-image registration (Japan Association on Remote Sensing, 1996). However, correlation analysis can also be used to measure the degree of relationship between two variables. In this paper two correlation coefficients, the correlation coefficient, r, (Equation 4) and the cross-correlation coefficient, cr, (Equation 5) have been used to analyze the level of correlation between the pre- and post- event images.

$$r_{mn} = \frac{\left(\sum_{j=1}^{ws}\sum_{i=1}^{ws} a_{ij}b_{ij}\right)^2}{\sum_{j=1}^{ws}\sum_{i=1}^{ws} a_{ij}^2 \sum_{j=1}^{ws}\sum_{i=1}^{ws} b_{ij}^2}, \qquad (4)$$

$$cr_{mn} = \frac{\sum_{j=1}^{ws}\sum_{i=1}^{ws}(a_{ij} - \mu_a)(b_{ij} - \mu_b)}{\left[\sum_{j=1}^{ws}\sum_{i=1}^{ws}(a_{ij} - \mu_a)\right]^{1/2}\left[\sum_{j=1}^{ws}\sum_{i=1}^{ws}(b_{ij} - \mu_b)\right]^{1/2}} \quad (5)$$

where:

r_{mn} = correlation coefficient of the (m, n) position of the moving window,

ws = window size for the computation of the correlation index,

a_{ij} = digital number of the (i, j) pixel of the post-event image,

b_{ij} = digital number of the (i, j) pixel of the pre-event image,

μ_a = mean value of all pixels within the referenced window of the post-event image,

μ_b = mean value of all pixels within the referenced window of the pre-event image, and

cr_{mn} = cross-correlation coefficient of the (m, n) position of the moving window.

From the correlation indices between the pre- and post-event images, new images are generated called correlation images. To accomplish this objective a square-shape moving window of size *ws* (being *ws* an odd number) is moved pixel by pixel and in each position (m, n) the correlation and cross-correlation indices are calculated, and thus generating the corresponding new pixel value for the correlation image, as schematized in Figure 9. The correlation and cross-correlation indices were calculated for each one of the bands of the pre- and post-event enhanced images, bands red, green and blue. The moving window's sizes, 3x3, 5x5 and 7x7 pixels were utilized.

It is expected that those sectors with higher level of damage present a lower value of correlation, due to changes in their reflectance, and contrarily higher values of correlation may suggest no changes between the images, indicating low levels of damage. After the correlation images were obtained, the mean value and standard deviation of the correlation values for each sector were calculated; they are shown in Figure 10. Figures 10(a), (b) and (c) show the mean value of the correlation for each sector for each band with the different window sizes. As it can be observed there is clear tendency of the values of correlation. As it was expected, lower values of correlation indicate areas of with high level of damage whereas values near the unit belong to the zones of minor damage. But in spite of this clear tendency of the values of correlation, we cannot be so sure in the identification of the different levels of damage since, as it can be appreciated in Figures 10(d), (e) and (f), the values of the standard deviation appear considerably high.

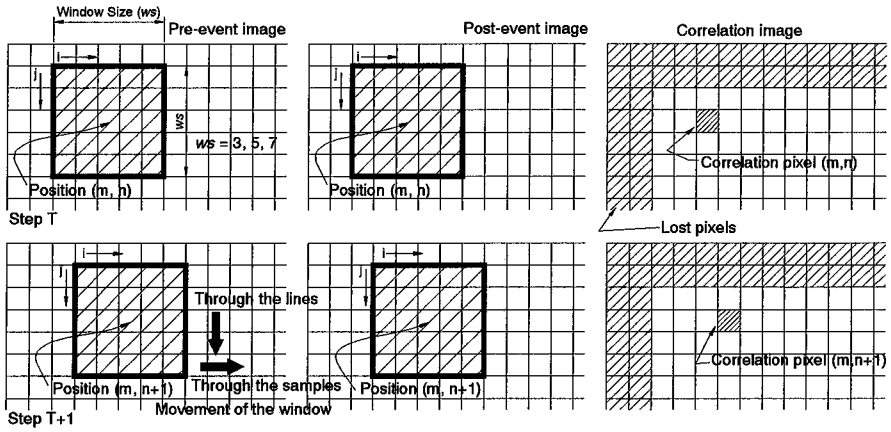

Figure 9. A square-shape window is moved sequentially pixel-by-pixel to the right up to the last possible position and then brought it back to the left and moved one line down and so on. In each position of the window the correlation and cross-correlation are computed.

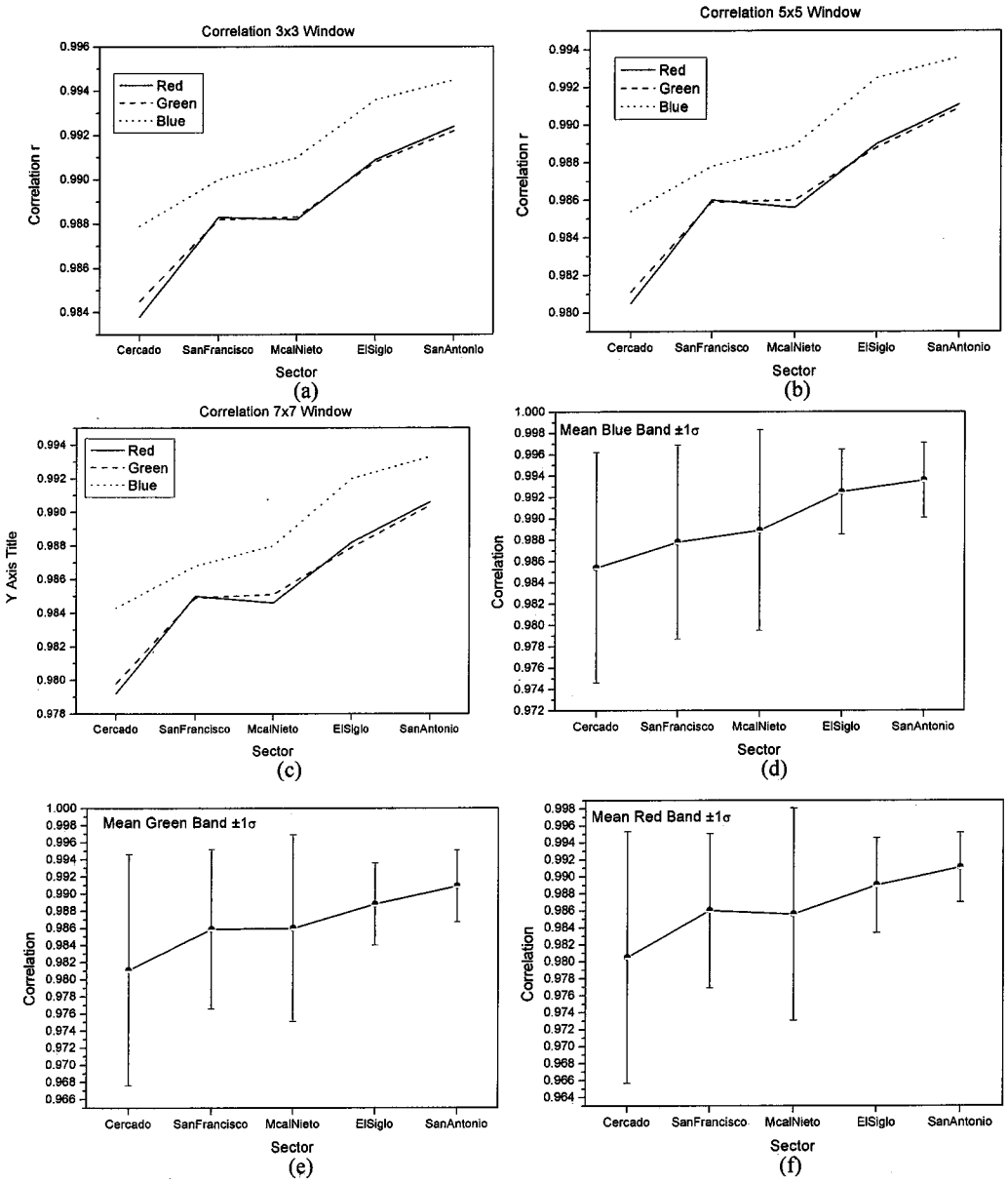

Figure 10. Mean value of the correlation r for different window sizes (a), (b) and (c), and mean value and standard deviation of the correlation value with 5x5 pixels window size for three bands (d), (e) and (f).

As for the cross-correlation coefficient there is not clear tendency with respect to the damage level. As it can be seen in Figure 11, the Cercado sector has a low value of correlation, followed by a high value for the sector of San Francisco, after this ambiguity there is tendency towards lower values of correlation that increase again in the zone of less damage in Figures 11(b) and (c). This behavior of the correlation coefficient requires a further investigation.

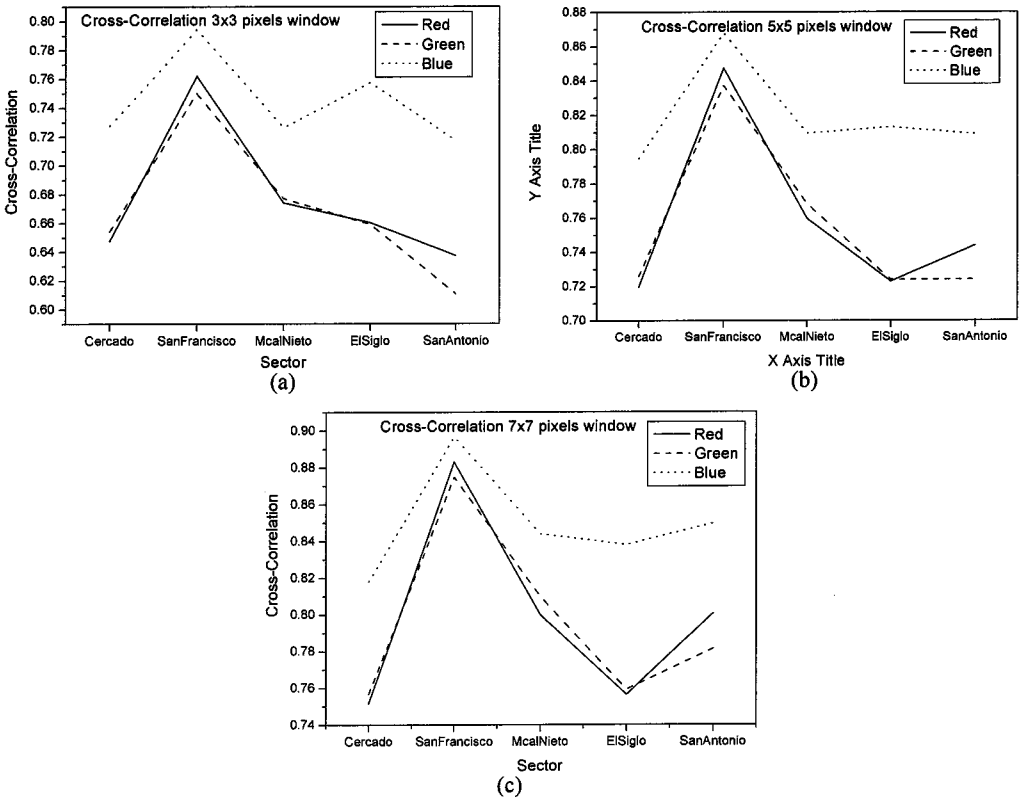

Figure 11. Mean value of the cross correlation *cr* for different window sizes.

Principal Component Analysis

The principal component transformation is designed to reduce redundancy in multispectral data. The purpose is to compress all of the information contained in an original *n*-bands data set into fewer *m* new bands or *components*. Let $L=\{L_1(DN_k), L_2(DN_k)\}$ be a combined set of $2n$ bands images composed of two different dates images and C_L be the variance-covariance matrix of L. Each principal component X_j is expressed as:

$$X_j = \sum_{k=1}^{n} \alpha_k L_1(DN_k) + \sum_{k=1}^{n} \beta_k L_2(DN_k) \tag{6}$$

where $\{\alpha_k, \beta_k\}$ is the normalized eigenvectors of the variance-covariance matrix C_L of L. Difference of the surface reflectance between two dates is evaluated by the following principal component:

$$D = \sum_{k=1}^{n} \alpha_k L_1(DN_k) + \sum_{k=1}^{n} \beta_k L_2(DN_k),\ (\alpha_k > 0, \beta_k < 0 \text{ for all } k) \tag{7}$$

In this case, by joining the 6 non-thermal bands of the pre- and post-event images, the set of $2n$ is obtained. In this study the 4th principal component satisfies the condition given by Formula 7, where the first 6 coefficients are positives and the lasts 6 are negative (Table 3). It means, this principal component conveys the changes between the pre- and post-event images for this multi-temporal set of images. The mean value and standard deviation of the pixels values of the 4th principal component are shown in Figure 12. As it can be seen, mean values show tendency from lower values of heavily damage areas increasing along the lower level of damage, however notice that there is a discontinuity in El Siglo sector as well as large values of the standard deviation.

Table 3. Values of the eigenvectors for the multi-temporal set of images. As it can be observed the 4th eigenvector satisfies the condition given by Equation 7.

Eigenvec	Band 1	Band 2	Band 3	Band 4	Band 5	Band 6	Band 7	Band 8	Band 9	Band 10	Band 11	Band 12
1	0.1666	0.2187	0.3399	0.3346	0.3026	0.2878	0.1716	0.2271	0.3550	0.3491	0.3172	0.3050
2	-0.1642	-0.1645	-0.3000	0.5307	0.1110	-0.0867	-0.1946	-0.2011	-0.3638	0.5661	0.0878	-0.1250
3	-0.1726	-0.1853	-0.1645	-0.2148	0.3704	0.3925	-0.2273	-0.2458	-0.2338	-0.2859	0.3864	0.4167
4	**0.2115**	**0.2297**	**0.2929**	**0.2987**	**0.3607**	**0.3371**	**-0.0743**	**-0.1484**	**-0.3092**	**-0.3149**	**-0.3656**	**-0.3574**
5	0.3410	0.1834	-0.2655	0.3886	-0.1647	-0.2661	0.3299	0.1182	-0.3271	-0.4037	0.2752	0.2493
6	0.2901	0.0980	-0.3504	-0.4684	0.2656	0.1948	0.4056	0.2305	-0.2930	0.3356	-0.0159	-0.1980
7	0.2787	0.1733	0.3167	-0.1758	-0.4852	0.1670	-0.1370	-0.2519	-0.3884	0.3055	-0.1325	0.3921
8	0.0911	0.1997	0.3902	-0.2457	0.1718	-0.4568	-0.2092	-0.0834	-0.1858	0.0391	0.5558	-0.3247
9	-0.5248	-0.0945	0.3734	-0.0213	0.1936	-0.2309	0.3114	0.3191	-0.4098	0.0142	-0.2198	0.2641
10	-0.3745	0.0713	0.0777	0.0753	-0.4751	0.4893	0.1388	0.2080	-0.1527	-0.0681	0.3796	-0.3785
11	-0.1359	0.5399	-0.2533	-0.0293	0.0224	-0.0123	-0.5730	0.5154	-0.0593	-0.0039	-0.1119	0.1197
12	-0.3876	0.6475	-0.1619	-0.0489	0.0493	-0.0617	0.3082	-0.5267	0.1352	0.0384	-0.0367	0.0463

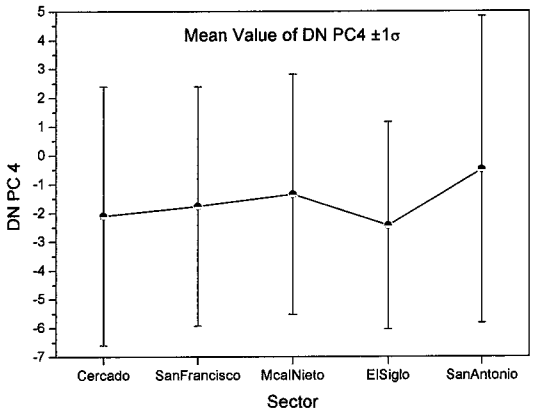

Figure 12. Mean values of the 4th principal component. Heavy damage sectors have lower pixel values increasing towards the sectors of less damage, however there is a discontinuity for this tendency at El Siglo sector.

Concluding Remarks

For the detection of damage due to the 2001 Atico, Peru earthquake, three methods have been applied: rationing, image correlation for the enhanced images, and principal component analysis. All of them showed some tendency in the behavior of the pixel values that constitute the new processed images. In case of rationing, places with high damage showed values greater than 1 and for less damage areas values near to 1. For the correlation method, sectors with high damage showed lower values of correlation while correlation values near to 1 were obtained for minor damage places. In case of principal component analysis, heavy damage sectors showed lower values than less damage areas. In case of this earthquake the clearest tendency has been observed in the image correlation method. However, particularly in this case, due to the large values of the standard deviation, there is not a high level of confidence to decide whether a pixel belong a damage area or not. In spite of the heavy damage in certain sectors, the changes in the post-event image were not much notable; the change of the contrast of the images was not as high as it was expected. A quick field survey was conducted one month after the earthquake to verify the condition in situ. As has been mentioned before, the most of houses that suffer heavy damage or collapse are those made of adobe (brick made of mud and straw) whose reflectance did not vary much after the earthquake. Because Moquegua City has dry climate, the wind may bring dust everywhere in the city, making the place with low contrast for the satellite sensors. All these factors made a clear distinction between damage and non-damage areas difficult, and hence a later image classification based on level of damage was not possible.

A further research will be conducted for the detection of damage using satellite images obtained by other sensors. We believe that the use of remotely sensed images is a promising technique for a fast and reliable tool for the assessment of level and extent of damage due to natural disasters.

Acknowledgement

The authors would like to thank to "Japan-Peru Center for Earthquake Engineering and Disaster Mitigation" (CISMID), for providing some statistical information about the damage in Moquegua City. The Landsat images were provided by USGS and NASDA. The "Earthquake and Tsunami disaster mitigation in the Asia and Pacific region (EQTAP)" project, sponsored by Ministry of Education, Culture, Science and Technology of Japan, supported to obtain the satellite images. The University of Tokyo supported the reconnaissance trip. Dr. Masashi Matsuoka of Earthquake Disaster Mitigation Research Center, National Research Institute for Earth Science and Disaster Prevention (EDM/NIED) for his helpful advise.

References

Campbell, J. (1996). *Introduction to Remote Sensing.* Second Ed. The Guilforf Press. USA.

Estrada, M., M. Kohiyama, M. Matsuoka and F. Yamazaki (2001). Detection of Damage Due to the 2001 El Salvador Earthquake Using Landsat Images. Proceedings of the 22nd Asian Conference on Remote Sensing, Volume 2, pp. 1372-1377. Singapore.

Estrada, M., M. Matsuoka and F. Yamazaki (2001). Digital Image Detection due to the 1999 Kocaeli, Turkey Earthquake. Bulleting of the Earthquake Resistant Structure Research Center, No. 34, pp. 55-66.

INCEDI, Instituto Nacional de Defensa Civil (2001). http://www.indeci.gob.pe

Japan Association on Remote Sensing (1996). *Remote Sensing Note.* Japan Association on Remote Sensing. Japan.

Kohiyama, M., H. Hayashi, N. Maki and, S. Hashitera (2000). Validity Study of EDES Application to Taiwan Chi-Chi Earthquake Disaster. Proceedings of the 21st Asian Conference on Remote Sensing, Volume 1, pp. 407-412. Taiwan.

Lillesand, T. M. and R. W. Kiefer (2000). *Remote Sensing and Image Interpretation.* John Wiley & Sons, Inc. USA.

Mather, P. M. (1999). *Computer Processing of Remotely-Sensed Images An Introduction.* Second Ed. John Wiley & Sons Ltd. England.

Matsuoka, M. and F. Yamazaki (2000). Remote Sensing Technologies for Earthquake Damage Detection: Examples for Kobe, Japan and Luzon, the Philippines. Workshop on Mitigation of Earthquake Disaster by Advanced Technologies (MEDAT-1). Los Angeles, USA.

Schowengerdt R. (1997). *Remote Sensing, Models and Methods for Image Processing.* Second Ed. Academic Press. USA.